

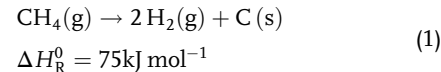
Methane Pyrolysis in a Liquid Metal Bubble Column Reactor: A Model Approach Combining Bubble Dynamics with Byproduct and Soot Formation

Neele Uhlenbruck,* Benjamin Dietrich, Christoph Hofberger, Leonid Stoppel, and Thomas Wetzel

Methane pyrolysis is a promising bridging technology to mitigate the effects of climate change. By decarbonizing natural gas, hydrogen can be produced from fossil fuels without creating CO₂ emissions. The focus of future process optimization should not only be on the hydrogen yield and the energy efficiency but also on the carbon products and possible byproduct formation. During methane pyrolysis in a liquid metal (LM) bubble column reactor, at least two very distinct types of carbon are synthesized: soot particles and graphene-like carbon sheets. A model is presented that couples a description of bubble dynamics in a LM bubble column reactor with a kinetic mechanism, originally developed for the combustion of natural gas that includes byproduct and soot formation. The model is validated by comparing it with an experimental dataset that covers a broad range of process conditions and the implications for carbon and byproduct formation are discussed. The good agreement of model results and experimental data shows that the combustion kinetic mechanism may be applied to methane pyrolysis and that the selected way of modeling bubble fluid dynamics in LM results in a good estimation of the actual bubble residence time in the optically nonaccessible liquid.

1. Introduction


The most recent report of the Intergovernmental Panel on Climate Change (IPCC) highlights the importance of taking action to mitigate the effects of climate change. Among others, the application of carbon capture and storage (CCS) technologies for the continued use of fossil energy sources and the production of “low-emission hydrogen” is suggested.^[1] Methane pyrolysis presents a means to decarbonize natural gas for the production of hydrogen according to the slightly endothermic and frequently used net reaction given in Equation (1).



Since no CO₂ is generated as in other processes like steam methane reforming, methane pyrolysis does not require conventional CCS. Yet, in addition to hydrogen, solid carbon is formed which may lead to clogging of the reactor tube^[2] or deactivation of solid metal catalysts by coke deposition on their surface,^[3,4] thus making uninterrupted hydrogen production difficult. The use of a liquid metal (LM) bubble column reactor provides a solution to circumvent the problem of carbon deposition and the continuous operation of an according pyrolysis reactor could be demonstrated.^[5,6] Because of its lower density, the pyrolytic carbon accumulates as a loose powder on the LM surface from where it can then be separated. Subsequently, it could either be permanently stored or used for industrial applications with long-term storage perspective, for example, as an additive for concrete production.^[7] Covering the global hydrogen demand of ≈90 Mt in 2020^[8] by methane pyrolysis would result in so much carbon produced as a byproduct that the market would probably be supersaturated.^[4,8] Thus, storage options have to be considered as well. Both for the safe storage and for the use of the pyrolytic carbon in industrial applications, a high carbon purity and low level of contaminants is desirable. The presence of yellow deposits, presumably polycyclic aromatic hydrocarbons (PAHs), has been reported after pyrolysis experiments.^[5] The formation of PAHs as an unwanted byproduct in combustion processes prior to soot formation under fuel-rich conditions^[9,10] and

N. Uhlenbruck, C. Hofberger, L. Stoppel
Karlsruhe Liquid Metal Laboratory (KALLA)
Institute for Thermal Energy Technology and Safety (ITES)
Karlsruhe Institute of Technology (KIT)
76344 Eggenstein-Leopoldshafen, Germany
E-mail: neele.uhlenbruck@kit.edu

B. Dietrich, T. Wetzel
Institute of Thermal Process Engineering (TVT)
Karlsruhe Institute of Technology (KIT)
76131 Karlsruhe, Germany

 The ORCID identification number(s) for the author(s) of this article can be found under <https://doi.org/10.1002/ente.202200654>.

© 2022 The Authors. Energy Technology published by Wiley-VCH GmbH. This is an open access article under the terms of the Creative Commons Attribution-NonCommercial-NoDerivs License, which permits use and distribution in any medium, provided the original work is properly cited, the use is non-commercial and no modifications or adaptations are made.

DOI: 10.1002/ente.202200654

as intermediate products during chemical vapor deposition (CVD) of carbon^[11] is well known. Many of these substances are a matter of concern due to their carcinogenic nature.^[12] Therefore, the aim of further process improvement should not only be the increase of the hydrogen yield but also the limitation of the PAH content of the solid products. To achieve these objectives, a better understanding of the processes inside the LM bubble column reactor is necessary. However, the opaque nature of the LM poses a major obstacle for the observation of the gas bubbles and the chemical processes inside them. This prevents the use of optical measurement methods, such as laser-induced incandescence (LII), that are typically employed during combustion experiments to analyze soot formation.^[13] In addition, the determination of the residence time presents a major challenge when the rise of the gas bubbles in the LM cannot be observed. A numerical model can help to shed light on these fluid dynamic and chemical processes and to optimize the reactor design in future studies.

Several attempts have been made during the past decade to model methane pyrolysis, both in conventional and in LM bubble column reactors. Geißler et al.^[5] developed a thermochemical model that focuses on the analysis of temperature effects in an LM bubble column reactor. They compared experimental data with model results obtained with different kinetic approaches for methane pyrolysis without byproduct formation, describing the reaction from Equation (1). They made several simplifying assumptions regarding bubble dynamics, for example, a constant bubble diameter over the entire height of the reactor, neglecting the increase of the bubble volume due to the change in hydrostatic pressure and the pyrolysis reactions. Furthermore, the initial bubble radius was calculated based on a force balance, which should not be applied under the conditions considered, as we are going to discuss later.

In a recent study, Catalan and Rezaei^[14] modeled methane pyrolysis in an industrial-scale LM bubble column reactor. They determined kinetic parameters based on experimental data from literature to describe Equation (1), additionally taking into account the thermodynamic equilibrium of the reaction. They have not considered byproduct formation, either, and assumed that mainly graphitic carbon is formed during uncatalyzed methane pyrolysis. However, examples from the industry, such as the established thermal black process, show that the uncatalyzed thermal decomposition of natural gas can be exploited for the production of carbon black, that is, intentionally produced soot particles with industrially designed properties. We are also going to show that one of the main types of carbon found in the pyrolytic carbon powder produced in a LM bubble column reactor is carbon black or soot. From this, a shortcoming of Equation (1) becomes evident: soot particles still contain a significant amount of hydrogen but the simplifying equation of the reaction assumes pure carbon to form so that all hydrogen atoms from the initial methane molecules are finally converted into hydrogen gas. Alfè et al.^[15] report H/C ratio as high as 0.3 for young soot particles from a methane flame and 0.2 for mature ones. Dobbins et al.^[16] found H/C ratio of about 0.17 for mature soot particles from ethylene flame. Therefore, kinetic approaches describing the CH₄ decomposition according to Equation (1), such as the ones by Catalan and Rezaei^[14] and Geißler et al.^[5] employed for their models, may succeed in describing the CH₄ conversion X_{CH_4}

accurately. However, predicting the hydrogen yield Y_{H_2} based on these calculations, assuming hydrogen selectivity $S_{\text{CH}_4, \text{H}_2}$ to be unity as in Equation (1) and neglecting both byproduct formation and the hydrogen content of soot, is expected to introduce a significant error. As one of the aims of further process optimization, as discussed in Section 1, should be to increase hydrogen yield, the accurate model prediction of H₂ production is crucial. This not only concerns the amount of hydrogen but also the required residence time. Kinetic approaches describing methane decomposition according to Equation (1) neglect the complex chemical network, finally leading to soot formation by a stepwise dehydrogenation of increasingly large hydrocarbons.^[9] Depending on the process conditions, there can be a significant time lag between methane consumption and carbon formation. The time lag is less pronounced for H₂ due to continuous dehydrogenation. H₂ is nevertheless not produced simultaneously to methane consumption in stoichiometric amounts matching Equation (1). In addition, kinetics describing only the consumption of methane cannot be used for the process optimization taking into account not only hydrogen yield but also the reduction of the PAH content of solids.

Fau et al.^[17] presented a numerical comparison of several kinetic mechanisms, both for pyrolysis and for combustion of hydrocarbons, to include the formation of byproducts during methane pyrolysis in an ideally mixed, isothermal, and isobaric batch reactor (BR). They limited the validation of the mechanisms to two datasets from literature; however, these cover only a very small range of pyrolysis conditions. One of the sets could not be modeled to a satisfactory level, while the agreement with the other was better for some of the mechanisms considered. Overall, they attribute the deviations to the experimental data, to the kinetic mechanisms not being extensive enough and the challenge of accurately representing the experimental conditions.

In the present work, a revised fluid dynamic model comprising bubble formation and bubble rise in a LM bubble column reactor is presented to overcome the difficulty of determining the residence time in the opaque—and therefore optically nonaccessible—LM. The bubble dynamics are coupled with a detailed chemical reaction mechanism from literature, originally developed for the combustion of natural gas that includes the formation of intermediates, such as PAHs, and soot particles. The model is validated for a broad range of operating conditions by comparing it with experimental data previously obtained under 64 different operating conditions.^[18] A special emphasis is placed on the formation of byproducts and process conditions under which we found Equation (1) to be oversimplifying.

2. Mathematical Modeling

The following section presents a mathematical model of an LM bubble column reactor with reactant gas inlet through a single orifice at the bottom of the reactor. The model combines both bubble dynamics to describe the formation and rise of the bubbles through the LM and chemical reaction kinetics. Several correlations for the initial equivalent bubble diameter and the bubble rise velocity are compared and discussed. The bubble column reactor can be divided into two parts, which

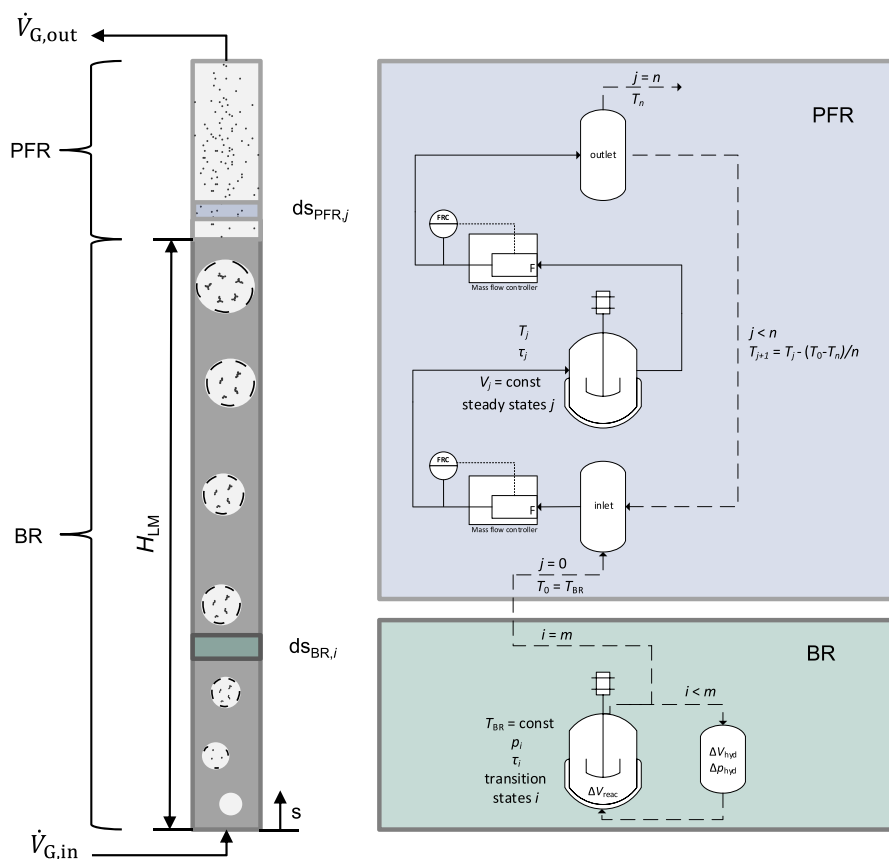


Figure 1. Schematic of the LM bubble column reactor and its discretization. A bubble in the lower part of the reactor is represented by an ideally mixed BR. The upper gas filled part is modeled as an ideal PFR.

are then discretized, as shown in the schematic of the reactor model in **Figure 1**.

The lower part of the reactor where bubble formation at the single orifice ($d_o = 0.5$ mm) and bubble rise take place in the liquid tin ($H_{Sn} = 1.05$ m) is divided into slices of $ds_{BR} = 0.01$ m. The gas is considered to show ideal behavior and the bubbles to be isothermal. The latter approximation is based on the previous analysis performed by Geißler et al.^[5] They analyzed that for an initial bubble diameter of 3 mm, the temperature at the center of the bubble reaches the temperature of the surrounding LM T_{LM} almost instantaneously. However, their assumption of a 3 mm bubble is based on bubble formation according to Tate's law, which is not applicable and underestimates the initial bubble diameter at the gas volume flows considered here, as will be shown. For larger bubble diameters of up to 10 mm, Geißler et al.^[5] concluded that the bubble center heats up within 0.3 s at LM temperature of only 1173 K, when heat-consuming reactions are very slow. At a higher T_{LM} of 1373 K and thus higher reaction rates, they calculated a significant delay in heating up the center of the bubble. Their analysis has to be considered a worst-case approximation, though. As they already stated, it only includes heat conduction, neglecting the internal gas circulation caused by the rise of the bubble.^[19] A further factor expected to improve the overall heat transfer inside the bubble, especially at high T_{LM} , is radiation absorbed by the black carbon particles once they are

formed. According to the model presented here, at 1373 K and pure methane as reactant gas, first soot particles are expected to form already at residence times as low as 0.13 s. Furthermore, Geißler et al.^[5] set the initial gas temperature of the bubble to only 298 K. Temperature measurements inside the glass tube leading to the single orifice at the bottom of the reactor showed that the gas is preheated to temperatures of ≈ 873 –1173 K immediately before a bubble is formed. This reduces the time needed to heat up a bubble significantly compared with the worst-case estimation presented by Geißler et al.^[5] The possible initiation of pyrolysis reactions directly before and during bubble formation is not part of the model discussed here as the gas residence time at relevant temperatures during bubble formation is negligible compared with the overall residence time as shown later.

Taking all the aforementioned aspects into account—that are expected to significantly reduce the time until the bubble center is heated up to T_{LM} compared with the estimation given by Geißler et al.^[5]—bubbles of an initial diameter of up to 10 mm are considered to have an isothermal temperature of T_{LM} once they are formed. As shown in **Figure 2**, for initial gas volume flows of about $\dot{V}_{G,0} \leq 300 \text{ mL}_N \text{ min}^{-1}$, the initial bubble diameters lie in this range according to all correlations considered. Therefore, for the following analysis and model validation, bubbles are assumed isothermal under all operating conditions presented in the Experimental Section.

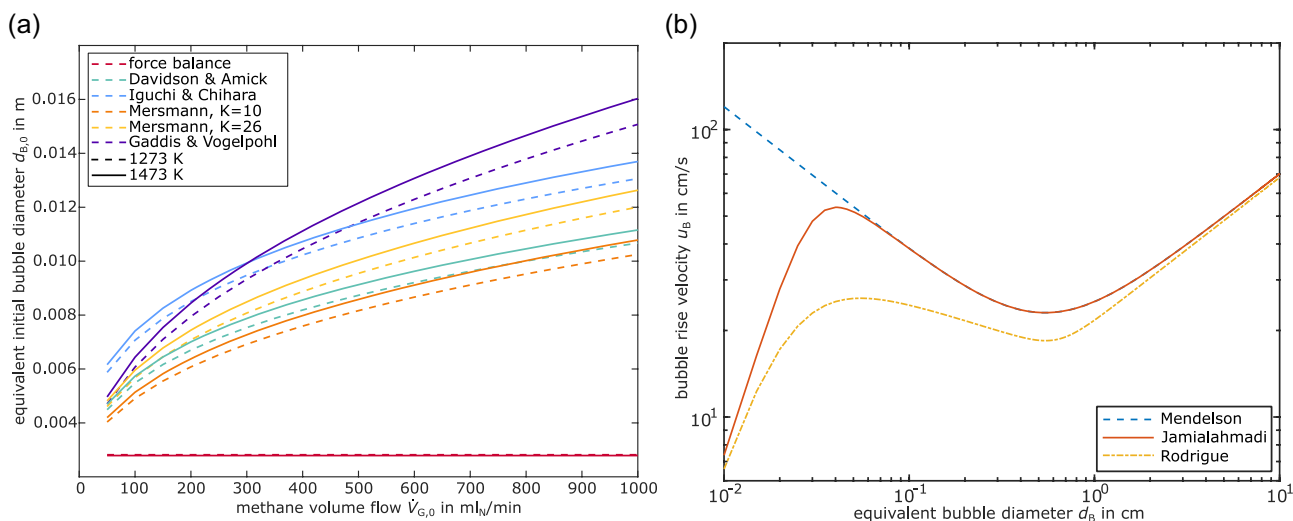


Figure 2. a) Comparison of correlations for the gas volume flow-dependent equivalent initial diameter $d_{B,0}$ of bubbles formed at a single orifice ($d_o = 0.5$ mm) in liquid tin and b) for the rise velocity u_B of bubbles in liquid tin ($T_{LM} = 1373$ K) depending on their equivalent diameter d_B .

As the bubbles rise, their volume increases due to the pyrolysis reactions taking place and the decrease of the hydrostatic pressure. No bubble coalescence is considered in the model. A single bubble is implemented in Python Cantera 2.5.1^[20] as an isothermal, constant pressure BR with the CRECK reaction mechanism for the combustion of natural gas including soot formation.^[21–24] Reactions are assumed to take place only in the reactor volume whereas the reactor surface, that is, the bubble interface, is considered inert. Upham et al.^[25] screened several LMs and metal alloys with regard to their catalytic activity in methane pyrolysis. They found the catalytic activity of pure liquid tin to be very low. Therefore, for the current model, the simplifying assumption is made that the catalytic contribution of the bubble interface to the pyrolysis reactions is negligible. However, the CRECK reaction mechanism^[21–24] includes reactions between gas-phase molecules and soot species, which, among others, lead to the formation of methyl radicals and H_2 . As in this reaction mechanism, solid soot particles are treated as pseudosppecies^[22] along with the gas-phase species; by default Cantera includes them in the gas density calculation, thus overestimating the actual gas density. This affects the residence times needed for the integration of the BR in the LM-filled part of the reactor but especially in the upper gas-filled part. Therefore, after each discretization step, a gas density correction is applied to obtain corrected bubble rise velocities and residence times. The volume of the selected type of reactor is adjusted according to volume changes by reaction but not due to changes in the hydrostatic pressure Δp_{hyd} . The adjustment of the pressure p_i inside the BR, which is assumed to equal the pressure in the LM at the same height of the reactor, is performed according to Equation (2) after each discrete volume element. The pressure at the surface of the LM p_{surf} is assumed constant and the local hydrostatic pressure $p_{hyd,i}$ takes into account the temperature-dependent material properties of liquid tin.

$$p_i = p_{surf} + p_{hyd,i} \quad (2)$$

Then, also the reactor volume V_i is increased by applying the ideal gas law. The total height of the LM is kept constant and independent of the gas hold up.

In order to calculate the equivalent initial diameter $d_{B,0}$ of spherical methane bubbles formed in liquid tin, a detailed comparison and evaluation of several correlations from literature is necessary. Based on the classification of bubble formation correlations published by Sano and Mori,^[26] only correlations for small gas chamber volumes and low-to-intermediate gas flow rates have been included in the analysis. Sano and Mori^[26] classified three correlations as applicable under these conditions: for very low gas flow rates, the bubble diameter can be obtained by a force balance also known as Tate's law, that is, by equilibrating the buoyancy and the surface tension force.^[27] For intermediate gas flow rates, Sano and Mori^[26] suggest a correlation given by Davidson and Amick,^[28] while for both cases they cite a correlation published by Mersmann.^[29] In addition, correlations later published by Gaddis and Vogelpohl^[30] and by Iguchi and Chihara^[31] were taken into consideration. The development of the equivalent initial bubble diameter $d_{B,0}$ at the orifice according to these correlations is depicted in Figure 2a for an increase of the gas volume flow $\dot{V}_{G,0}$ from 50 to 1000 mL_N min⁻¹. The results were obtained for pure methane bubbles formed at a single orifice with a diameter of $d_o = 0.5$ mm in liquid tin at $T_{LM} = 1273$ K and $T_{LM} = 1473$ K. As shown, the influence of the temperature is small compared with the influence of the gas volume flow for all correlations but the force balance, which is independent of the volume flow. As the latter is only applicable for very low volume flows, it underestimates the initial bubble diameter for the full range of gas flows considered here. The correlation of Gaddis and Vogelpohl^[30] yields bubble formation frequencies in the range of 35–43 Hz for the experimental operating conditions described in the Experimental Section. Calculating the frequencies based on the force balance would lead to even higher frequency values, as the predicted initial bubble diameters are significantly smaller than the ones obtained

from the other correlations analyzed. Sano and Mori^[26] give an upper limit of 1.67 Hz for the applicability of Tate's law. Therefore, the force balance approach clearly should not be used to obtain the initial bubble diameter under the experimental conditions presented in Section 5.

With respect to the correlations of Davidson and Amick^[28] as well as Iguchi and Chihara,^[31] the opposite is the case. These two correlations are based on experimental volume flow rates that exceed 200 mL_N min⁻¹^[31] or where the experimental conditions presented in Section 5 are located at the very lower end of the range the correlation covers.^[28] Furthermore, Davidson and Amick^[28] derived their empirical correlation for air bubbles in water and mineral oil, without including the effect of material properties like the liquid density or surface tension. Both properties have been observed to influence bubble formation, especially for rather low gas volume flows,^[32,33] and differ greatly for liquid tin and water.^[34–36] On the contrary, Iguchi and Chihara^[31] explicitly analyzed bubbles in LM and therefore their correlation is expected to give a good approximation for bubble formation in LM for higher gas volume flows than experimentally considered here. From the remaining two correlations, the one presented by Gaddis and Vogelpohl,^[30] which is given by Equation (3), is chosen to model the initial bubble diameter for several reasons. Mersmann^[29] used a parameter K to fit his correlation to different experimental datasets. Depending on the data, he considered K ranges from 10 to 26. This leads to an increasing deviation in the resulting bubble diameters at higher volume flows, as shown in Figure 2a. It is not clear which value of K should be used for bubbles formed in liquid tin and whether the value of K for liquid tin even lies within the range given by Mersmann.^[29] Sarrafi et al.^[27] compared several correlations and noted the best agreement of the correlation of Gaddis and Vogelpohl^[30] for both a single orifice and several orifices, which is an important factor for a possible model-based scale-up of the LM bubble column reactor. Kulkarni and Joshi^[32] concluded as well that the correlation of Gaddis and Vogelpohl^[30] describes bubble formation best. In addition, with regard to scale-up and higher volume flows, considering the viscosity of the liquid becomes more important,^[33] which is not included in Mersmann's correlation.^[29] Furthermore, Keplinger et al.^[37] found the correlation of Gaddis and Vogelpohl^[30] to be in good agreement with gas bubbles formed in LM for gas volume flows ranging from 10 to 1200 mL_N min⁻¹, thus covering both gas volume flows relevant for the experimental values presented here as well as for a possible scaleup.

$$d_{B,0} = \left[\left\{ \frac{6d_o\sigma_L}{\rho_L g} \right\}^{\frac{1}{3}} + \left\{ \frac{81\nu_L \dot{V}_G}{\pi g} \right\} + \left\{ \frac{135 \dot{V}_G^2}{4\pi^2 g} \right\}^{\frac{1}{5}} \right]^{\frac{1}{4}} \quad (3)$$

The temperature-dependent surface tension of liquid tin is calculated according to Gancarz et al.^[35] while correlations for the density and viscosity of liquid tin are given by Assael et al.^[34] With the initial bubble diameter $d_{B,0}$ and the volume flow at the orifice $\dot{V}_{G,0}$ the bubble formation time τ_B can be calculated according to Equation (4).

$$\tau_B = \frac{V_{B,0}}{\dot{V}_{G,0}} = \frac{\frac{\pi}{6} d_{B,0}^3}{\dot{V}_{G,0}} \quad (4)$$

A comparison of the bubble formation time τ_B for the conditions considered here with the time τ_{LM} the bubble takes to rise to the surface of the LM showed that $\tau_B/\tau_{LM} < 0.004$. Therefore, the bubble formation time is not considered for further modeling and the residence time in the LM-filled part of the reactor is set to τ_{LM} . The total ascension time τ_{LM} of a bubble is the sum of all differential residence times $d\tau_{LM,i}$. $d\tau_{LM,i}$ is calculated for each discrete section of the LM-filled part of the reactor as the quotient of the discrete height ds_{BR} and the local bubble rise velocity $u_{B,i}$ according to Rodrigue's correlation^[38] given in Equation (5)–(7).

$$u_B = V \left(\frac{\sigma_L \eta_L}{\rho_L^2 d_B^2} \right)^{\frac{1}{3}} \quad (5)$$

$$V = \frac{F}{12} \left[\frac{\left(1 + 1.31 \times 10^{-5} M^{\frac{11}{20}} F^{\frac{73}{33}} \right)^{\frac{21}{176}}}{\left(1 + 0.020 F^{\frac{10}{11}} \right)^{\frac{10}{11}}} \right] \quad (6)$$

$$F = g \left[\frac{\rho_L^5 d_B^8}{\sigma_L \eta_L^4} \right]^{\frac{1}{3}} \quad (7)$$

Rodrigue^[38] based the correlation on a large number of experimental observations, among which are also several values obtained for bubbles in LM. The range of validity is based on the Reynolds number Re and the Morton number M . For the system considered here, the range of relevant Reynolds numbers agrees with the scope given by Rodrigue.^[38] In case of the Morton number, the value of approximately $M \approx 4.7 \times 10^{-15}$ for the modeled system is one order of magnitude smaller than the scope of $3.62 \times 10^{-14} < M < 9.4 \times 10^4$ covered by Rodrigue's correlation.^[38] As an alternative, a correlation presented by Mendelson^[39] and a later addition to this correlation for very small bubbles by Jamialahmadi et al.^[40] have been considered. However, their authors do not give a range of validity. The bubble rise velocities obtained according to all three correlations for different bubble diameters in liquid tin at a temperature of $T_{LM} = 1373$ K are shown in Figure 2b. Only one temperature is depicted as the temperature dependence of the bubble rise velocity is very small. For large bubble diameters, the correlations agree fairly well, but Rodrigue's correlations yields lower bubble rise velocities for small bubble diameters, such as the ones expected in the LM bubble column reactor. Besides the given range of validity, Rodrigue's correlation^[38] yielding lower rise velocities $u_{B,i}$ is chosen for the model presented here due to an observation Wang et al.^[41] made which may lead to a reduction of $u_{B,i}$. They noticed that particles attached to the outside of a bubble slow down its rise velocity by stabilizing the surface of the bubble and reducing oscillations. They observed a stronger effect for a larger amount of particles. Although the carbon particles formed during methane pyrolysis are located inside the gas bubbles, they might have a similar effect. Hozumi et al.^[19] observed and modeled the transport of dispersed solid particles inside gas bubbles to the gas–liquid interface. Therefore, the pyrolytic carbon particles can be expected to be at least partially attached to the inner surface of the bubbles.

For bubble columns with small inner diameter, the interaction between the rising bubbles and the reactor walls has to be considered.^[42,43] For this purpose, Clift et al.^[43] suggest the multiplication of the bubble rise velocity with a wall factor WF. As no coalescence is considered in the model, bubbles comply over the entire length of the reactor with the range of validity given by Clift et al.^[43] The bubble Eotvos number Eo_B is smaller than 40 and the ratio of the equivalent bubble diameter and the inner reactor diameter $\lambda = \frac{d_B}{d_R}$ yields values <0.6 . Then WF can be calculated according to Equation (8),^[43] leading to a reduction of u_B by $\approx 3.3\%–7\%$ for the model conditions considered here.

$$WF = [1 - \lambda^2]^{1.5} \quad (8)$$

As the bubble wall interaction intensifies for larger bubbles, a stronger reduction of u_B is modeled to occur at higher temperatures, leading to higher CH_4 conversions, at higher initial CH_4 concentrations and toward the surface of the LM, as all this provokes an increase of the bubble volume.

An ideal plug flow reactor (PFR) without gas back mixing, which is divided into differential slices of $ds_{\text{PFR}} = 0.002$ m, represents the upper part of the reactor above the LM surface. At the LM surface, the pressure p_{surf} is set to 1.1 bar. The PFR is implemented in Cantera^[20] as a cascade of $n_{\text{PFR}} = 100$ ideally mixed steady-state gas reactors (CSTRs). The temperature of these reactors is adjusted for each discretization step following a linear temperature gradient from the LM surface with T_{LM} to the gas outlet as given in Equation (9).

$$T_j = T_{j-1} - \Delta T_{\text{PFR}} = T_{j-1} - \frac{T_{\text{LM}} - T_{\text{G,out}}}{n_{\text{PFR}}} \quad (9)$$

T_1 of the first CSTR is already lower than T_{LM} by ΔT_{PFR} and the temperature decreases by ΔT_{PFR} for each further step j before the integration of the reactor to steady state. At the upper end of the reactor, the gas exits with a temperature of $T_{\text{G,out}} = 373$ K and a pressure of 1 atm. The gas velocity is calculated for the gas leaving each discrete reactor slice. All soot particles formed during the process are carried out of the reactor with the gas mixture as a first model approximation. The total mass fraction of soot y_{soot} is calculated as the sum of mass fractions of all-soot-particle species included in the reaction mechanism.^[22]

To reduce the computing time, the reaction mechanism for natural gas combustion^[21–24] has been reduced down to the $R = 10\,000$ most relevant reactions and $K = 333$ most relevant species, among which several are PAHs, as described in another study.^[44] The full mechanism is designed to model methane combustion but for pyrolysis, for example, reactions including oxygen do not have to be considered. For the reduction of the reaction mechanism, the following conditions were chosen: $T = 1473$ K, $p = 1$ bar, an integration time of 1 s and the initial reactant gas composition was set to $\text{CH}_4:\text{N}_2:\text{H}_2:\text{CO}_2$ with a ratio of 5:2:1:2 to include reactions taking place under different dilution conditions. To determine the number of relevant reactions to be included, ideal gas reactors with a range of start conditions (10%–100% CH_4 with varying amounts of N_2 , H_2 , CO_2 at $p = 1$ bar and T between 1323 and 1673 K) and reduced reaction mechanisms including 5000, 8000, 10 000, and 23 000 reactions

respectively have been integrated over 1 s. The comparison of the different reduction scenarios shows hardly any deviation between 10 000 and 23 000 reactions. For the main gas-phase reactive species, CH_4 and H_2 , a reduction down to only $R = 5000$ reactions and $K = 273$ species already gives a good approximation. With $R = 8000$ reactions and $K = 300$ species included in the mechanism, the main species show already good agreement with deviations becoming more obvious at high temperatures. Looking at the formation of the largest soot aggregate (BIN25CJ) though, there is still a noticeable deviation from the full reaction mechanism at only $R = 8000$ reactions. The deviation $\Delta y_{\text{BIN25CJ},R}$ from results obtained with 23 000 reactions can be reduced significantly by increasing the amount of reactions considered to 10 000 (e.g., at 1200 °C, 100% CH_4 : $\Delta y_{\text{BIN25CJ},8000} = 1.323\%$ vs. $\Delta y_{\text{BIN25CJ},10000} = -0.025\%$).

3. Model Validation and Discussion

To validate the model, calculated gas mole fractions \bar{y}_i at the reactor outlet have been compared with results obtained by gas chromatograph (GC) analysis for the species i listed in the description of the experimental setup at the end.

3.1. Main Reactive Gas-Phase Species

Regarding the main reactive gas-phase species CH_4 and H_2 , modeled values of \bar{y}_{CH_4} and \bar{y}_{H_2} have been checked against the corresponding mole fractions from datasets obtained at 64 different experimental operating conditions, as shown in **Figure 3**.

The data points depicted in **Figure 3** are given in Table S1 and S2, Supporting Information. For better recognizability of single data points, error bars have not been included. As shown in **Figure 3**, there is an overall excellent agreement of the modeled mole fractions and experimentally obtained data for CH_4 and H_2 . The maximum absolute deviation $\Delta \bar{y}_{\text{CH}_4, \text{max}} = 3.53\%$ is found at 1100 °C for 50 $\text{mL}_N \text{min}^{-1}$ and 100% CH_4 as reactant gas, while a minimum absolute deviation of $\Delta \bar{y}_{\text{CH}_4, \text{min}} = 0.07\%$ is reached at 1100 °C for 200 $\text{mL}_N \text{min}^{-1}$ with 50% CH_4 in N_2 . For H_2 , the modeled values differ slightly less from the experimental values than for CH_4 . In spite of the very good agreement under almost all operating conditions, \bar{y}_{CH_4} is overestimated by the model. This can be seen more clearly, when the experimental and the modeled methane conversions X_{CH_4} are compared as in **Figure 4a**.

A transmission electron microscopy (TEM) analysis of the cumulative carbon sample reveals a possible explanation for the discrepancy between modeled and experimental methane conversions: While the pyrolytic carbon powder contains many typical soot aggregates, such as the one in **Figure 5a**, there are also large graphene-like carbon sheets present (see **Figure 5b**). Currently, no conclusions regarding the quality and layer number of these carbon sheets can be drawn. For simplicity, they will be referred to as “graphene” in the following discussion.

As the reaction mechanism only takes into account the formation of soot particles, the modeled methane conversion is likely to be too low because graphene growth on the gas–liquid interface of the bubbles as an additional sink for carbon atoms is

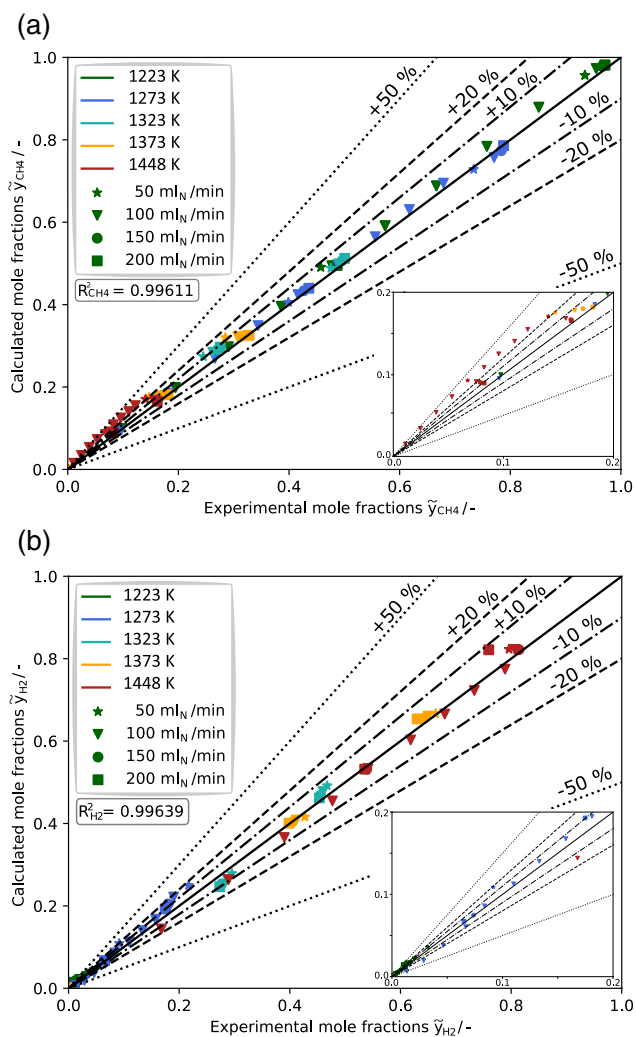


Figure 3. a) Comparison of modeled and experimentally determined mole fractions \tilde{y}_{CH_4} and b) \tilde{y}_{H_2} at the reactor outlet. The total reactant gas flow rates at the reactor inlet were varied from 50 to 200 mL_N min⁻¹, represented by different symbols, and contained 10 to 100 vol% CH₄, diluted with N₂ where applicable. The LM temperature T_{LM} was varied from 1223 to 1448 K, represented by the different colors of the symbols.

neglected. Comparable temperatures and high methane dilution rates have been reported for graphene growth by CVD on LM surfaces.^[45,46] Figure 5c shows a schematic of the simplified mechanisms that are assumed to occur inside a methane bubble, leading to soot and graphene formation. Of the mechanisms depicted in Figure 5c, which is meant to illustrate in a very simplified manner a possible explanation for the observation of the two very distinct types of carbon species shown in Figure 5a,b, the numerical model presented here currently only comprises soot formation. For the model calculations presented, as a simplifying assumption, the liquid–metal interface is treated inert as discussed in Section 2.

For methane pyrolysis in the temperature range considered here, the abstraction of the first hydrogen atom from the methane molecule, leading to the formation of CH₃ radicals, is

assumed the rate-determining step (RDS) of the reaction chain, leading to carbon formation after stepwise dehydrogenation of increasingly large hydrocarbons.^[47] Before soot nucleation from the gas phase and the subsequent growth and aggregation of the particles, large PAHs form by consecutive reactions.^[9,10] For graphene growth on (solid) metal substrates, small gas-phase species such as CH₄, C₂H₄, or C₂H₂ are common precursors. Dissociative chemisorption of these small molecules on a metal surface has been identified as an important initial step for CVD graphene growth.^[48] For CVD graphene growth from CH₄, chemisorption is probably followed by further dehydrogenation and dimerization reactions on the substrate surface, surface diffusion, and the formation of carbon clusters, leading to graphene nucleation and growth by carbon addition to the graphene edges.^[49,50] Graphene growth could be added to the reaction mechanism in a future study provided appropriate kinetic data for the processes involved in graphene growth on a liquid tin substrate under comparable process conditions are available. Cantera^[20] offers the possibility to include surface reactions and extend the applied reaction network accordingly. Many studies on graphene growth describe low-pressure conditions^[51] and if atmospheric pressure CVD is used, also with LM as substrates, methane is usually strongly diluted.^[45,51,52] The review by Muñoz and Gómez–Aleixandre^[51] shows the complexity of CVD graphene growth and the many factors influencing it. The properties of the substrate, for example, the solubility and diffusivity of carbon in it, play a crucial role in graphene growth, and applying different (solid) metal substrates already leads to significant differences in the prevailing mechanisms. Using LMs instead as a substrate affects the growth of graphene further, as important factors such as grain boundaries present in solid metal substrates as well as the crystalline structure do not exist anymore. Several authors^[45,53,54] mention faster surface diffusion of carbon species on LM compared with solid substrates. A deeper understanding of the relevant mechanistic steps with liquid tin as a substrate for CVD growth of graphene and comparably high partial pressures of methane is necessary to make sure all relevant processes would be included in a future extended model. Currently, the literature on graphene growth on LM known to the authors does not match the reaction conditions described here and does not provide the necessary kinetic data to include graphene growth on liquid tin in the model.

Looking at the modeled and the experimental hydrogen yield Y_{H_2} and the hydrogen $S_{\text{CH}_4, \text{H}_2}$ in Figure 4b,c, the importance of including the long reaction chain and the formation of byproducts during methane pyrolysis in the model become evident. According to Equation (1), pure carbon is formed from methane, while the modeled soot species still contain hydrogen atoms. During the aging of soot particles, dehydrogenation takes place, thus reducing the H/C ratio. Alfè et al. reported a decrease from ≈ 0.3 for young soot to 0.2 for mature soot formed in a methane flame.^[15] That is, hydrogen atoms remain clearly part of the soot structure even for mature soot particles. Therefore, simplifying carbon formation during methane pyrolysis according to Equation (1), and neglecting both the H content of the soot particles as well as by-product formation, is expected to lead to an overestimation of hydrogen yield. Exactly this is shown in Figure 4b, where the theoretical values of Y_{H_2} have been

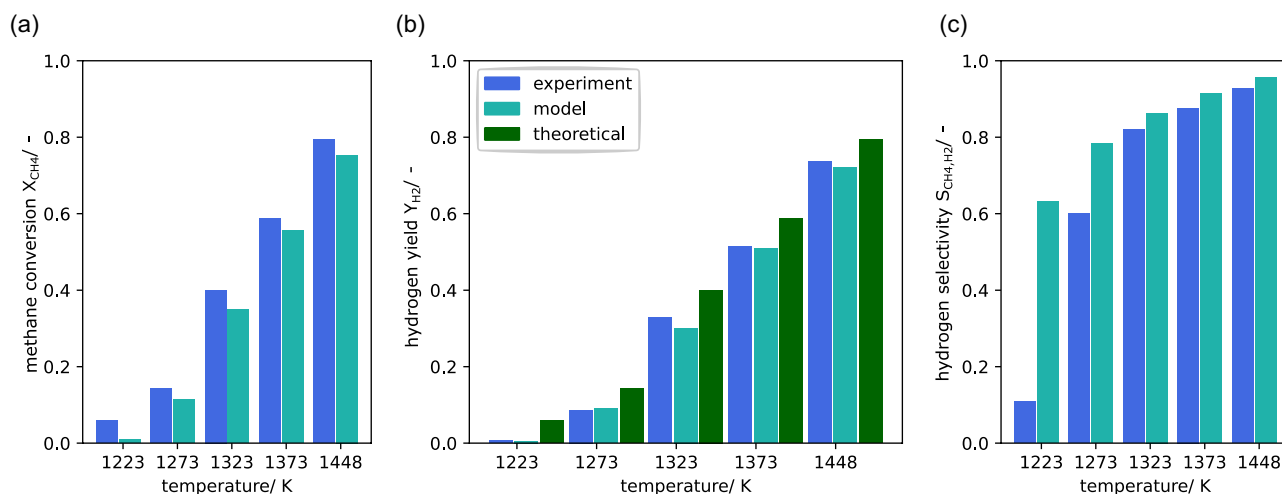


Figure 4. a) Modeled and experimental methane conversion X_{CH_4} , b) hydrogen yield Y_{H_2} , and c) hydrogen selectivity S_{CH_4,H_2} at various LM temperatures T_{LM} , $\dot{V}_{C,O} = 100 \text{ mL}_N \text{ min}^{-1}$, and a 1:1 reactant gas mixture of CH_4 and N_2 .

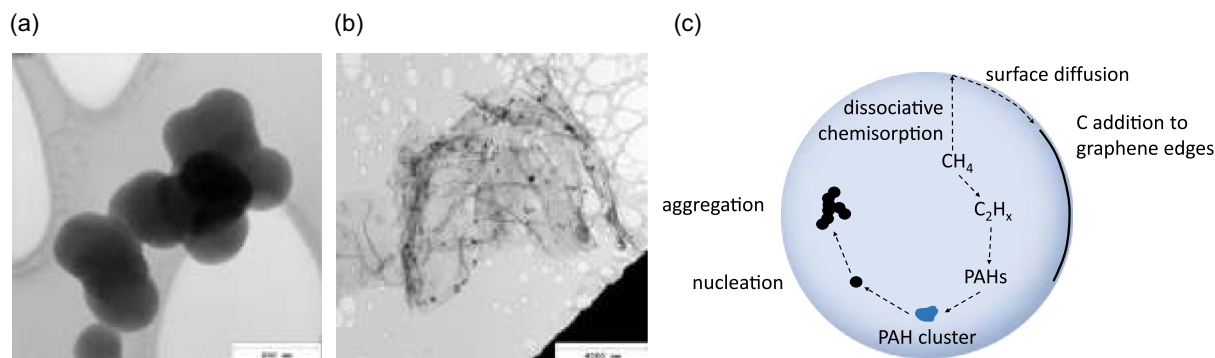
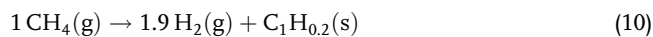


Figure 5. Different types of carbon formed during methane pyrolysis in an LM bubble column reactor: a) Soot particles and b) graphene-like carbon sheets mixed with soot particles. c) Schematic of simplified mechanisms leading to the formation of the two types of carbon inside a gas bubble.

calculated based on Equation (1) and the experimental methane conversions shown in Figure 4a. If a kinetic approach for the reaction rate of methane during pyrolysis, such as the ones applied by Catalan and Rezaei^[14] and by Geißler et al.^[5] succeeds in describing the consumption of methane correctly, the calculated methane conversions would match the experimental results and hydrogen yields might be estimated according to Equation (1). The hydrogen yields thus obtained lead to significant deviations, overestimating the model and experimental results presented in Figure 4b. The application of Equation (1) requires a hydrogen selectivity of the reactor S_{CH_4,H_2} close to unity. This however is only given approximately at the highest T_{LM} considered here, as shown in Figure 4c. The lower the T_{LM} , the more S_{CH_4,H_2} deviates from unity, as soot formation and dehydrogenation are incomplete with many byproducts such as PAHs present. As the modeled methane conversion at 1223 and 1273 K is significantly lower than the experimental one, and S_{CH_4,H_2} is the ratio of Y_{H_2} and X_{CH_4} , the calculated hydrogen selectivities exceed the experimental ones, in spite of the excellent agreement of model and experiments regarding hydrogen

yield. The conclusion of these observations, both the higher experimental methane conversion and the significantly lower hydrogen selectivity, is that during the experiments, at low pyrolysis temperatures more byproducts were formed than predicted by the model. When PAH clusters start to form soot particles, a drop in the H/C ratio has been observed,^[16] resulting in a significant release of hydrogen. In addition, soot is known to age, meaning that young particles usually contain more H than old ones as at high temperatures; over time, further dehydrogenation and graphitization takes place.^[15,16,55] However, the low hydrogen yields and very low experimental selectivity, especially at 1223 K, suggest that no or hardly any soot formation takes place. The pyrolysis reactions finally leading to soot formation are very slow at 1223 K and probably only advance far enough to form PAHs. The H/C ratio of PAHs is higher than for soot particles, so these molecules can “store” a lot of hydrogen, thus strongly reducing hydrogen selectivity. The actual PAH content of the pyrolysis products synthesized at low T_{LM} is therefore expected to be higher than the modeled amount of PAHs. On the other hand, at the highest temperature level of 1448 K, the pyrolysis

reactions have advanced far enough to consume intermediates almost completely. Without byproducts and an H/C ratio of 0.2 for soot particles produced from methane,^[15] which corresponds to a fictitious hydrogen-containing carbon species $C_1H_{0.2}$ instead of just C in the simplified case of pure carbon, the stoichiometry of Equation (1) can be modified to yield Equation (10).



From Equation (10), a maximum hydrogen selectivity $S_{\text{CH}_4, \text{H}_2}$ of 0.95 results, which is very close to the experimental value of 0.928 and the model value of 0.957 shown in Figure 4c. So even if at 1448 K no full methane conversion was achieved, the PAH content of the solid products synthesized under these conditions could be expected to be very low. Looking at the improved prediction of hydrogen yield shown in Figure 4b and the conclusions regarding byproduct formation that can be drawn from the hydrogen selectivity, the presented model could be a good starting point for the design of a hydrogen production plant. Especially the higher hydrogen yields at the more elevated temperatures considered would be of interest, where the deviations seen in Figure 4a–c are smaller than for the lower temperature levels. However, for the scale-up of the reactor to industrial scale, possible changes in the fluid dynamics of the bubble column would have to be considered and implemented to obtain a good estimation of the residence time.

3.2. Minor Gas-Phase Species

Regarding the minor gas-phase species, there is a very good agreement between model and experiment with respect to acetylene. No C_2H_2 has been detected by GC analysis and the model predicts only tiny amounts of $<<0.1\%$ for the three highest temperature levels while the predicted amounts of $\tilde{y}_{C_2H_2}$ get close to 0.1% for some of the initial $\tilde{y}_{\text{CH}_4,0}$ considered at the two lower temperatures, as shown in Table S5,

Supporting Information. Only for 50% CH_4 in N_2 at 1273 K and initial volume flows of $150 \text{ mL}_N \text{ min}^{-1}$ ($\tilde{y}_{C_2H_2} = 0.136\%$) and $200 \text{ mL}_N \text{ min}^{-1}$ ($\tilde{y}_{C_2H_2} = 0.160\%$) mole fractions of C_2H_2 are predicted that slightly exceed the limit of quantification of 0.1%—according to the documentation provided by the manufacturer—of the GC that was used to obtain the experimental data as described in the Experimental Section 5.

During the experiments, C_2H_6 was only detected under certain conditions with concentrations being mostly $<0.1\%$. The only exceptions, where higher concentrations of C_2H_6 were observed, are at 1273 and 1323 K for 100% CH_4 . At 1323 K, there seems to be a temperature-dependent maximum as shown in Figure 6a which is also present in the model predictions although the model clearly overestimates $\tilde{y}_{C_2H_6}$ at all temperature levels. This is the opposite of what Pejpichestakul et al.^[22] reported for C_2H_6 in sooting methane flames when they describe and validate the kinetic mechanism applied here. They noticed an underestimation of C_2H_6 while the formation of C_2H_4 in the flames they analyzed was predicted too high. The differing trends could be caused by the complete absence of oxygen and oxygen-containing species in the pyrolysis model and experiments presented here. In addition, Pejpichestakul et al.^[22] compare the maximum concentrations of these species predicted by their model to maximum values determined in flames, whereas here the modeled concentrations at the reactor outlet are compared with experimental data. Currently, for the methane pyrolysis model presented here, no conclusion as to the accuracy of maximum concentrations occurring over the length of the reactor can be drawn, as the LM bubble column reactor is not optically accessible because of the opacity of the liquid tin.

Of the C_2H_x species ($x = 2, 4, 6$), the highest concentrations were detected for C_2H_4 , so for this side product of methane pyrolysis, the experimental trends can be analyzed a bit more thoroughly. Experimental and model results regarding the influence that temperature has on $\tilde{y}_{C_2H_4}$ for an initial volume flow of $100 \text{ mL}_N \text{ min}^{-1}$ and reactant gas mixtures of 100% CH_4 and 50% CH_4 in N_2 are shown in Figure 6a. The data points both in

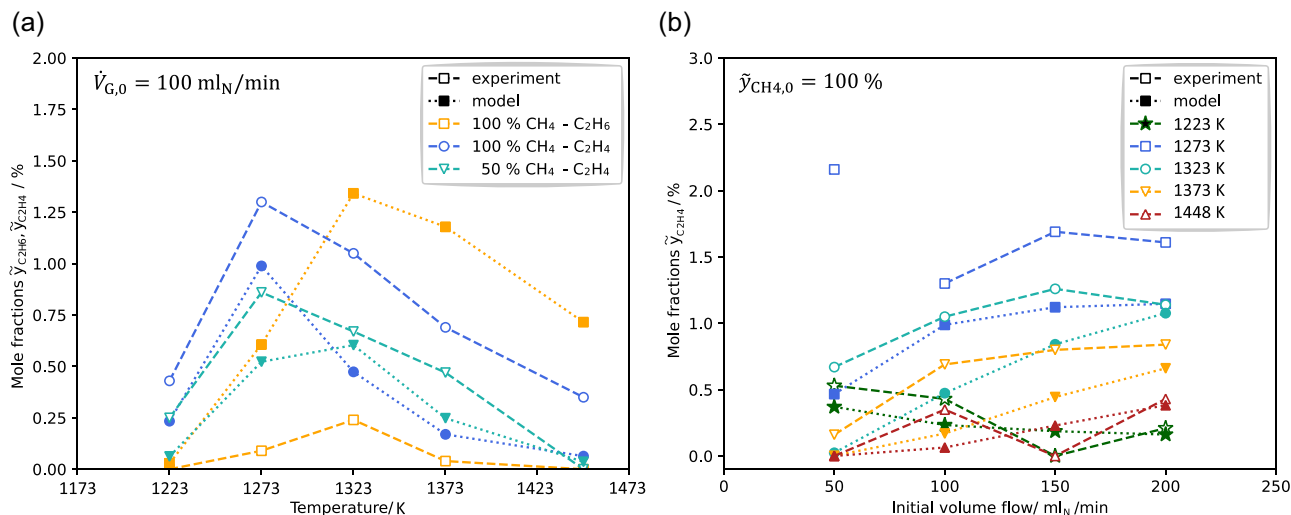


Figure 6. a) Comparison of modeled and experimental influence of temperature and b) initial volume flow on side product mole fractions.

Figure 6a,b have been connected with trend lines to guide the eye. Both the experimental values and the model display a tendency of $\tilde{y}_{C_2H_4}$ to decrease with an increase in temperature after reaching a maximum at 1273 K. However, for 50% CH₄ in N₂ the model predicts this maximum to occur at 1323 K. The experimental and model mole fractions of the C₂H_x species at the reactor outlet for the different reactant flowrates and LM temperatures are given in Table S3–S5, Supporting Information.

Figure 6b displays the influence of the initial volume flow on the final mole fraction of C₂H₄. Modeled and experimental values are in good agreement, both showing an overall increase of $\tilde{y}_{C_2H_4}$ for higher volume flows. Looking at the general trend, the authors consider the experimental mole fraction at 1273 K and 50 mL_N min⁻¹ an outlier. However, this assumption should be tested in further experiments.

In total, the model yields a very good quantitative representation of the major gas-phase species. In addition, the C₂H_x side products are predicted well. Even though currently some of the relative errors for the side species are high, the general model predictions regarding the influence of temperature and volume flow on the C₂H_x species match experimental results quite well.

4. Conclusion

A numerical simulation approach for methane pyrolysis in a LM bubble column reactor has been presented. It is based on combining a model for the dynamics of bubble formation and ascension in LM with a reaction mechanism,^[21–24] originally developed for methane combustion that includes byproduct and soot formation. For the fluid dynamic part of the model an extensive analysis of various correlations for the determination of both the initial bubble diameter and the bubble rise velocity was performed. The correlation given by Gaddis and Vogelpohl^[30] for the initial bubble diameter and Rodrigue's correlation^[38] for the bubble rise velocity has been selected. The model approach has been validated by comparison with experimental data covering a broad range of reactant gas compositions and LM temperatures. Modeled and measured mole fractions of the main species CH₄ and H₂ are in excellent agreement. In addition, the model results obtained for C₂H_x side species match the experimental trends well. This shows that the kinetic mechanism for the combustion of natural gas may also be applied to describe methane pyrolysis. Furthermore, the good agreement indicates that the fluid dynamic modeling represents the bubble formation and rise in LM to a satisfactory level, thus overcoming the challenge of determining the residence time of a bubble in an opaque medium. An analysis of the temperature-dependent methane conversion, hydrogen yield, and hydrogen selectivity illustrates the importance to include byproduct formation into models of methane pyrolysis. A deficit of simpler kinetic approaches, describing the decomposition of methane only, is the overestimation of the amount of hydrogen produced based on the stoichiometry of Equation (1), as the hydrogen content of soot and the formation of byproducts with high H/C ratios are neglected. Deriving the hydrogen production based on methane consumption would only be a valid approximation when the hydrogen selectivity S_{CH_4, H_2} is close to unity, whereas the model and

Table 1. Experimental operating conditions. N₂ was used as diluent gas.

$T_{LM,ref}$	1223, 1273, 1323, 1373, 1448 K
$\dot{V}_{G,0}$	50, 100, 150, 200 mL _N min ⁻¹
$\tilde{y}_{CH_4,0}$ at 1323, 1373 K and all $\dot{V}_{G,0}$	0.5, 1.0
$\tilde{y}_{CH_4,0}$ at 1223, 1273, 1448 K and 100 mL _N min ⁻¹	0.1 ... 1.0, $\Delta\tilde{y}_{CH_4,0} = 0.1$

the experimental data presented here show that this does not apply at lower pyrolysis temperature levels. Only at the highest pyrolysis temperature of 1448 K considered in this work, the amount of byproducts is shown to be negligible. Over the whole range of process conditions, the model predictions for methane conversion tend to be slightly too low. A TEM analysis of a cumulative carbon sample produced and collected under the various reaction conditions presented gives a possible explanation for this deviation: The sample not only contains soot aggregates, but also graphene-like carbon sheets.

5. Experimental Section

The experimental dataset used in this work stems from previous work by Geissler^[18] and was newly evaluated. Methane pyrolysis experiments were conducted in a LM bubble column reactor described in detail elsewhere.^[5,6,18,56] A quartz glass tube with an inner diameter of 40.6 mm and a length of 1268 mm was filled with liquid tin up to a height of $H_{Sn} = 1050$ mm (at 1273 K) without packed bed and heated by an electrical oven. The temperature inside the reactor was measured at several vertical positions by Type K thermocouples with the one at a height of $H_{Sn} = 600$ mm used to determine the LM reference temperature $T_{LM,ref}$. Reactant gas consisting of either 100 vol% methane 5.5 or 10–90 vol% methane diluted with nitrogen 6.0 was fed into the reactor via a single orifice ($d_o = 0.5$ mm) at the bottom of the quartz glass tube where bubbles formed. Flow controllers were used to adjust the reactant gas flow $\dot{V}_{G,0}$ to the orifice as well as the ratio of methane and nitrogen. During the rise of bubbles, methane thermally decomposed into mainly hydrogen and solid carbon. After leaving the reactor the pyrolysis gas was analyzed by a GC operating with argon as a carrier gas and equipped with a thermal conductivity detector and two columns (HayeSep N, molecular sieve 13X) for the detection of CH₄, H₂, C₂H₆, C₂H₄, C₂H₂, and N₂. Based on comparable recent GC measurements with the same analyzer, a worstcase estimation yielded an uncertainty of the GC dataset for H₂ and CH₄ in higher concentrations in the range of $\pm 3 \dots 6\%$. According to the information provided by the manufacturer, the limits of quantification (LoQ) for C_xH_y (with $x \leq 2$) and CO_x as well as N₂ and O₂ were 0.1 vol% and for hydrogen 0.001 vol%. Concentrations of C₂H_y getting close to the LoQ were estimated to have an uncertainty of $\pm 30 \dots 40\%$. The experimental operating conditions referred to latter for the validation of the model are given in Table 1. To generate the TEM images, the carbon sample was transferred onto a copper grid with a lacey carbon film and analyzed with a Philips CM200 FEG microscope at an acceleration voltage of 200 kV.

Supporting Information

Supporting Information is available from the Wiley Online Library or from the author.

Acknowledgements

This work was part of the project NECOC (Creation of Negative emissions by separating atmospheric CO₂ into economically usable Carbon black and

O₂) and was supported by the German Federal Ministry for Economic Affairs and Climate Action (BMWK) (grant number FKZ: 03EE5009A).
Open Access funding enabled and organized by Projekt DEAL.

Conflict of Interest

The authors declare no conflict of interest.

Data Availability Statement

The data that support the findings of this study are available from the corresponding author upon reasonable request.

Keywords

bubble column reactors, carbon black, graphene, liquid metals, pyrolysis

Received: June 23, 2022

Revised: September 9, 2022

Published online:

-
- [1] Intergovernmental Panel on Climate Change (IPCC), in *Climate Change 2022: Mitigation of Climate Change. Contribution of Working Group III to the Sixth Assessment Report of the Intergovernmental Panel on Climate Change* (Eds.: P. R. Shukla, J. Skea, R. Slade, A. A. Khourdajie, R. van Diemen, D. McCollum, M. Pathak, S. Some, P. Vyas, R. Fradera, M. Belkacemi, A. Hasija, G. Lisboa, S. Luz, J. Malley), Cambridge University Press, Cambridge, UK, NY **2022**, "Summary for Policymakers".
- [2] A. Abánades, E. Ruiz, E. M. Ferruelo, F. Hernández, A. Cabanillas, J. M. Martínez-Val, J. A. Rubio, C. López, R. Gavela, G. Barrera, C. Rubbia, D. Salmieri, E. Rodilla, D. Gutiérrez, *Int. J. Hydrogen Energy* **2011**, *36*, 12877.
- [3] N. Sánchez-Bastardo, R. Schlögl, H. Ruland, *Chem. Ing. Tech.* **2020**, *92*, 1596.
- [4] N. Muradov, T. Veziroglu, *Int. J. Hydrogen Energy* **2008**, *33*, 6804.
- [5] T. Geißler, M. Plevan, A. Abánades, A. Heinzl, K. Mehravarán, R. K. Rathnam, C. Rubbia, D. Salmieri, L. Stoppel, S. Stückrad, A. Weisenburger, H. Wenninger, T. Wetzel, *Int. J. Hydrogen Energy* **2015**, *40*, 14134.
- [6] T. Geißler, A. Abánades, A. Heinzl, K. Mehravarán, G. Müller, R. K. Rathnam, C. Rubbia, D. Salmieri, L. Stoppel, S. Stückrad, A. Weisenburger, H. Wenninger, T. Wetzel, *Chem. Eng. J.* **2016**, *299*, 192.
- [7] B. Han, S. Sun, S. Ding, L. Zhang, X. Yu, J. Ou, *Composites, Part A* **2015**, *70*, 69.
- [8] International Energy Agency (IEA), *Global Hydrogen Review 2021*, **2021**, <https://www.iea.org/reports/global-hydrogen-review-2021> (accessed: April 2022).
- [9] H. Richter, J. B. Howard, *Prog. Energy Combust. Sci.* **2000**, *26*, 565.
- [10] J. W. Martin, M. Salamanca, M. Kraft, *Prog. Energy Combust. Sci.* **2022**, *88*, 100956.
- [11] W. G. Zhang, K. J. Hüttinger, *J. Mater. Sci.* **2001**, *36*, 3503.
- [12] W. M. Baird, L. A. Hooven, B. Mahadevan, *Environ. Mol. Mutagen.* **2005**, *45*, 106.
- [13] H. A. Michelsen, *Proc. Combust. Inst.* **2017**, *36*, 717.
- [14] L. J. J. Catalan, E. Rezaei, *Int. J. Hydrogen Energy* **2020**, *45*, 2486.
- [15] M. Alfè, B. Apicella, R. Barbella, J.-N. Rouzaud, A. Tregrossi, A. Ciajolo, *Proc. Combust. Inst.* **2009**, *32*, 697.
- [16] R. A. Dobbins, R. A. Fletcher, H.-C. Chang, *Combust. Flame* **1998**, *115*, 285.
- [17] G. Fau, N. Gascoin, P. Gillard, J. Steelant, *J. Anal. Appl. Pyrolysis* **2013**, *104*, 1.
- [18] T. G. Geißler, Doctoral Thesis, *Karlsruhe Institute of Technology*, **2017**.
- [19] Y. Hozumi, Y. Yoshizawa, *Comput. Fluids* **1992**, *21*, 211.
- [20] D. G. Goodwin, R. L. Speth, H. K. Moffat, B. W. Weber, Cantera: An Object-oriented Software Toolkit for Chemical Kinetics, Thermodynamics, and Transport Processes. Version 2.5.1, **2021**, <https://www.cantera.org> (accessed: May 2021).
- [21] CRECK Modeling Group, C1-C16 HT + Soot + NOx mechanism. Version 2003, March 2020, <http://creckmodeling.chem.polimi.it/menu-kinetics/menu-kinetics-detailed-mechanisms/107-category-kinetic-mechanisms/412-mechanisms-1911-tot-ht-soot-nox> (accessed: May 2021).
- [22] W. Pejpichestakul, E. Ranzi, M. Pelucchi, A. Frassoldati, A. Cuoci, A. Parente, T. Faravelli, *Proc. Combust. Inst.* **2019**, *37*, 1013.
- [23] E. Ranzi, C. Cavallotti, A. Cuoci, A. Frassoldati, M. Pelucchi, T. Faravelli, *Combust. Flame* **2015**, *162*, 1679.
- [24] E. Ranzi, A. Frassoldati, A. Stagni, M. Pelucchi, A. Cuoci, T. Faravelli, *Int. J. Chem. Kinet.* **2014**, *46*, 512.
- [25] D. C. Upham, V. Agarwal, A. Khechfe, Z. R. Snodgrass, M. J. Gordon, H. Metiu, E. W. McFarland, *Science* **2017**, *358*, 917.
- [26] M. Sano, K. Mori, *Trans. Jpn. Inst. Met.* **1976**, *17*, 344.
- [27] A. Sarrafi, H. Müller-Steinhagen, J. M. Smith, M. Jamialahmadi, *Can. J. Chem. Eng.* **1999**, *77*, 11.
- [28] L. Davidson, E. H. Amick, *AIChE J.* **1956**, *2*, 337.
- [29] A. Mersmann, *VDI-Forschungsh.* **1962**, *491*, 28 B.
- [30] E. S. Gaddis, A. Vogelpohl, *Chem. Eng. Sci.* **1986**, *41*, 97.
- [31] M. Iguchi, T. Chihara, *Metall. Mater. Trans. B* **1998**, *29*, 755.
- [32] A. A. Kulkarni, J. B. Joshi, *Ind. Eng. Chem. Res.* **2005**, *44*, 5873.
- [33] M. Jamialahmadi, M. R. Zehataban, H. Müller-Steinhagen, A. Sarrafi, J. M. Smith, *Chem. Eng. Res. Des.* **2001**, *79*, 523.
- [34] M. J. Assael, I. J. Armyra, J. Brillo, S. V. Stankus, J. Wu, W. A. Wakeham, *J. Phys. Chem. Ref. Data* **2012**, *41*, 033101.
- [35] T. Gancarz, Z. Moser, W. Gąsior, J. Pstruś, H. Henein, *Int. J. Thermophys.* **2011**, *32*, 1210.
- [36] W. Wagner, H.-J. Kretzschmar, in *VDI-Wärmeatlas 11. Auflage*, (Eds: Verein Deutscher Ingenieure (VDI) - Gesellschaft Verfahrenstechnik und Chemieingenieurwesen (GVC)), Springer-Verlag, Berlin, Heidelberg, Germany **2013**, Ch. D2.1.
- [37] O. Keplinger, N. Shevchenko, S. Eckert, *Int. J. Multiphase Flow* **2018**, *105*, 159.
- [38] D. Rodrigue, *Can. J. Chem. Eng.* **2008**, *82*, 382.
- [39] H. D. Mendelson, *AIChE J.* **1967**, *13*, 250.
- [40] M. Jamialahmadi, C. Branch, H. Müller-Steinhagen, *Chem. Eng. Res. Des.* **1994**, *72*, 119.
- [41] P. Wang, J. J. Cilliers, S. J. Neethling, P. R. Brito-Parada, *Chem. Eng. J.* **2019**, *365*, 111.
- [42] T. Sirino, E. Mancilla, R. E. Morales, *Int. J. Multiphase Flow* **2021**, *145*, 103818.
- [43] R. Clift, J. R. Grace, M. E. Weber, *Bubbles, Drops, and Particles*, Academic Press, New York, NY **1978**.
- [44] Cantera, *mechanism_reduction.py*, https://cantera.org/examples/python/kinetics/mechanism_reduction.py.html (accessed: March 2022).
- [45] G. Ding, Y. Zhu, S. Wang, Q. Gong, L. Sun, T. Wu, X. Xie, M. Jiang, *Carbon* **2013**, *53*, 321.
- [46] M. Zeng, L. Tan, J. Wang, L. Chen, M. H. Rummeli, L. Fu, *Chem. Mater.* **2014**, *26*, 3637.
- [47] A. Holmen, O. Olsvik, O. A. Rokstad, *Fuel Process. Technol.* **1995**, *42*, 249.

- [48] H. C. Lee, W.-W. Liu, S.-P. Chai, A. R. Mohamed, A. Aziz, C.-S. Khe, N. M. S. Hidayah, U. Hashim, *RSC Adv.* **2017**, *7*, 15644.
- [49] W. Zhang, P. Wu, Z. Li, J. Yang, *J. Phys. Chem. C* **2011**, *115*, 17782.
- [50] H. Mehdipour, K. Ostrikov, *ACS Nano* **2012**, *6*, 10276.
- [51] R. Muñoz, C. Gómez-Aleixandre, *Chem. Vap. Deposition* **2013**, *19*, 297.
- [52] J. Wang, M. Zeng, L. Tan, B. Dai, Y. Deng, M. Rummeli, H. Xu, Z. Li, S. Wang, L. Peng, J. Eckert, L. Fu, *Sci. Rep.* **2013**, *3*, 2670.
- [53] J. Liu, L. Fu, *Adv. Mater.* **2018**, *31*, 1800690.
- [54] C. Tsakonas, M. Dimitropoulos, A. C. Manikas, C. Galiotis, *Nanoscale* **2021**, *13*, 3346.
- [55] M. R. Kholghy, A. Veshkini, M. J. Thomson, *Carbon* **2016**, *100*, 508.
- [56] L. Stoppel, T. Fehling, T. Geißler, E. Baake, T. Wetzel, *IOP Conf. Ser.: Mater. Sci. Eng.* **2017**, *228*, 012016.